Multiple Equilibria of a Double-Gyre Ocean Model with Super-Slip Boundary Conditions

FRANCOIS W. PRIMEAU

MIT/WHOI Joint Program in Oceanography, Cambridge, Massachusetts

ABSTRACT

The steady-state solutions of a barotropic double-gyre ocean model in which the wind stress curl input of vorticity is balanced primarily by bottom friction are studied. The bifurcations away from a unique and stable steady state are mapped as a function of two nondimensional parameters (δ_I, δ_S), which can be thought of as measuring respectively the relative importance of the nonlinear advection and bottom damping of relative vorticity to the advection of planetary vorticity.

A highly inertial branch characterized by a circulation with transports far in excess of those predicted by Sverdrup balance is present over a wide range of parameters including regions of parameter space where other solutions give more realistic flows. For the range of parameters investigated, in the limit of a large Reynolds number, $\delta_I/\delta_S \rightarrow \infty$, the inertial branch is *stable* and appears to be unique. This branch is antisymmetric with respect to the midbasin latitude like the prescribed wind stress curl. For intermediate values of δ_I/δ_S, additional pairs of mirror image nonsymmetric equilibria come into existence. These additional equilibria have currents that redistribute relative vorticity across the line of zero wind stress curl. This internal redistribution of vorticity prevents the solution from developing the large transports that are necessary for the antisymmetric solution to achieve a global vorticity balance. Beyond some critical Reynolds number, the nonsymmetric solutions are unstable to time-dependent perturbations. Time-averaged solutions in this parameter regime have transports comparable in magnitude to those of the nonsymmetric steady state branch. Beyond a turning point, where the nonsymmetric steady-state solutions cease to exist, all the computed time-dependent model trajectories converge to the antisymmetric inertial runaway solution. The internal compensation mechanism, which acts through explicitly simulated eddies, is itself dependent upon an explicit dissipation parameter.

1. Introduction and motivation

Numerical ocean models are an indispensable tool for understanding the climate system and possibly for predicting climate change. Ocean models are not only used in conjunction with observations to estimate the current state of the oceans, but also to estimate the state of the ocean under different mechanical and thermodynamical forcing. These models depend on boundary conditions and subgrid-scale parameterizations that are poorly known from observations. For climate studies, the time evolution of ocean models over hundreds to thousands of years is of paramount importance. This makes the choice of suitable parameterizations of dissipation rather crucial, since dissipative forces, no matter how small, have enough time to become important.

For the wind-driven ocean circulation, the subgrid-scale parameterization of mixing processes provides an explicit dissipation term in the governing equation. Ped-

losky (1996) reviews the role played by dissipation in theories of the wind-driven circulation within the context of homogeneous models. In all cases that have been studied, the explicit frictional dissipation is responsible for balancing the continuous input of vorticity by the action of the wind stress. The hope that as the boundary-layer Reynolds number is increased, the total circulation would become independent of the particular frictional model adopted has been disappointed. As demonstrated by Ierley and Sheremet (1995), in a single-gyre model with free-slip boundary conditions, a steady basin-filling inertial gyre with velocities far in excess of those predicted by Sverdrup balance is the only solution for a sufficiently large boundary layer Reynolds number.

Of particular interest to our study is the double-gyre simulation by Marshall (1984). In this model, a source of negative vorticity input by the curl of the wind stress in the southern region of the basin is balanced by a positive source of vorticity of equal magnitude in the northern region. Marshall's (1984) study stands out because it appears to provide an example in which time-dependent eddies prevent the development of the inertial runaway solution. In this simulation, the amount of negative vorticity put in by the wind in the subtropical gyre

Corresponding author address: Dr. Francois W. Primeau, Massachusetts Institute of Technology, Room 54-1511A, Cambridge, MA 02139-4307.
E-mail: fprimeau@mit.edu

is roughly balanced by the eddy flux of negative vorticity from the southern gyre to the northern gyre, thereby eliminating the need for the vorticity input by the wind to be eliminated in the western boundary layer. It is important to point out, however, as Pedlosky (1996) emphasizes, that this internal compensation mechanism can only apply for the singular case in which there is no net input of vorticity by the curl of the wind stress over the entire domain—any imbalance must be removed by the explicit dissipation.

Despite its limited applicability to the real ocean case, the internal compensation mechanism deserves further study since its action appears to make the time-averaged solutions independent of the explicit dissipation parameterization. In particular, one would want to know which type of instabilities allow the internal compensation mechanism to act and whether inertial runaway can be truly avoided as the boundary-layer Reynolds number is increased. The first motivation for this study is to address these issues.

To this end, we follow the method of Ierley and Sheremet (1995) and investigate steady-state solutions and their stability for a large range of parameters. The techniques of numerical bifurcation theory are used to unravel the bifurcation structure of the steady-state equilibria of the ocean model introduced by Marshall (1984). The model is essentially the same as that used in a study of steady-state solutions by Cessi and Ierley (1995) but differs in the choice of dissipation operator and boundary conditions; Cessi and Ierley (1995) used Munk-type lateral diffusion with free slip at the eastern and western walls and periodic boundary conditions at the northern and southern walls. This model's interesting novelty is that the boundary conditions are such that no relative vorticity flux is allowed through the basin walls, despite the fact that the model has both bottom friction and lateral diffusion. The boundary conditions are therefore dynamically equivalent to those of a model having bottom friction alone. The model nonetheless retains a lateral diffusion term that prevents the development of discontinuities in the relative vorticity field. This formulation of the boundary condition for the eddy diffusion term is based on the observation that geostrophic eddies act only to redistribute vorticity laterally and not as sink of vorticity through the basin walls. A discussion of this super-slip boundary condition, as well as other choices of boundary conditions, can be found in Pedlosky (1996).

By studying the steady-state solutions, we will discover in which region of parameter space the circulation retains the Sverdrup balance as part of the solution and in which part of parameter space the circulation is of the inertial runaway type. By studying the bifurcation structure of the steady-state solutions, we will map out where qualitative changes in the nature of the solution occur and thus carve out regions of parameter space where the internal compensation mechanism can act.

The second motivation for this study deals with the issues of low-frequency variability and multiple equilibria. As pointed out by Jiang et al. (1995), the oceans' western boundary currents offer clear examples of low-frequency variability in the wind-driven ocean circulation. Some examples are provided by the path of the Kuroshio alternating between a large and a small meander state with a period of several years (Taft 1972) by the latitude of separation of the Brazil/Malvinas current system varying on interannual timescales (Olson et al. 1988) and by the mean position of the Gulf Stream that varies interannually (Brown and Evans 1987). Interannual and longer timescale variability is a possible manifestation of the nonlinearity of the wind-driven circulation since it cannot be accounted for by the seasonal cycle of the forcing.

Because of the nonlinearity of the equations governing the oceans, oceanic currents can exhibit a rich variety of dynamical behaviors, including multiple equilibria, self-sustained oscillations, and chaos. Dynamical systems theory has been applied extensively to the thermohaline circulation because of its clear role in the earth's climate system: it transports large amounts of heat poleward. The gyre dynamics associated with the wind-driven circulation has received much less attention from the point of view of low-frequency variability and multiple equilibria. It is surely no less important, however. For example, the midlatitude gyres of the North Pacific are probably the main agents of poleward heat transport in that ocean, and in the North Atlantic the modeling study of Spall (1996a, b) has demonstrated how the surface wind-driven circulation can be coupled to the deep western boundary current and thus affect the strength of the thermohaline circulation. Using a primitive equation model of the Gulf Stream/deep western boundary current crossover, Spall (1996b) found low-frequency variability associated with the transition between two preferred dynamical states, which included a high energy state with the Gulf Stream extension penetrating deep into the basin and a low energy state with a weakly penetrating Gulf Stream extension. The mechanism controlling the transition between the two states involved the interaction between the surface wind-driven currents and the deep western boundary current.

In a simpler reduced gravity quasigeostrophic (QG) model of the double-gyre circulation, McCalpin and Haidgovel (1996) also found low-frequency variability. This low-frequency variability was associated with irregular transitions among several preferred dynamical regimes, including a high energy state with a jet penetrating deep into the basin, a low energy state with a weakly penetrating jet, and an intermediate energy state with intermediate jet penetration. Despite the differences between the models of Spall and McCalpin and Haidgovel, the preferred dynamical regimes were similar from one model to the other: the jet penetration scale and the intensity of the eddy energy field varied among states in a similar fashion for both models. Even though the mechanism for the transition between states

is different for the models, the similar nature of the preferred regimes suggest that the existence of these regimes might be the result of the dynamics of the wind-driven circulation alone. The preferred dynamical regimes are likely to be linked to unstable steady states, or fixed points, of the equations governing the wind-driven circulation. Studying the steady-state solutions of the simpler QG wind-driven model may lead to a better understanding of the dynamical balances that allow preferred dynamical states.

The ideas of dynamical systems theory can be used to investigate the low-frequency variability associated with the transition among different regimes. In general the fixed point solutions have associated with them a stable and an unstable manifold. Almost all trajectories that begin in a neighborhood of the fixed point are eventually expelled along the unstable manifold. These trajectories can, however, sometimes return to the neighborhood of the fixed point by following a trajectory close to the stable manifold. In this sense the unstable fixed points act to ''steer'' the trajectory of the time-dependent models (Legras and Ghil 1985), thus providing a mechanism for recurrent and persistent dynamical regimes.

Recently, several studies have introduced the concepts of attractors and fixed points to help characterize the behavior of wind-driven ocean models. For dissipative dynamical systems, all solutions converge, as $t \rightarrow \infty$, to a complicated set called the global attractor, which may be fractal. This set is, in general, finite dimensional and embodies the long time evolution of the model, including turbulent states. Although it is not yet numerically feasible to fully map out the global attractor of general circulation ocean models, it is possible to find their fixed points. These fixed points lie in the global attractor and can be useful in characterizing the long time evolution of the model. Recent work on the attractors of wind-driven ocean models is the study of Jiang et al. (1995) and of Speich (1995), who studied multiple equilibria of a wind-driven shallow-water model. Ierley and Sheremet (1995) studied multiple equilibria of a barotropic single-gyre wind-driven model. Meacham and Berloff (1997) and Berlof and Meacham (1997) studied the low-dimensional attractors of a single-gyre wind-driven model. Cessi and Ierley (1995) studied multiple equilibria of a barotropic double-gyre model with lateral diffusion and free-slip boundary conditions.

The above considerations make it crucial that the long time evolution ($t \rightarrow \infty$) of ocean models of varying complexity and with differing subgrid-scale parameterizations and boundary conditions be investigated in a systematic way for a wide range of parameter values. As a contribution toward this goal, we present in this study the fixed points and their stability properties for a wind-driven circulation model having a super-slip boundary condition.

The paper is organized as follows. In section 2 we formulate the model. In section 3 we discuss the multiple equilibria and their stability properties. In section 4 we give an overview of the bifurcation structure of the model. In section 5 we briefly summarize the results and provide a final discussion.

2. Model formulation

As mentioned in the introduction, the model configuration is the same as that used in Marshall (1984). The governing equation, in nondimensional form, is the barotropic vorticity equation with bottom friction and biharmonic lateral diffusion:

$$\frac{\partial \zeta}{\partial t} + \mathbf{u} \cdot \nabla q = \frac{1}{\pi} \nabla \times \tau - \delta_s \zeta - \delta_H^5 \nabla^4 \zeta \quad \text{in } \mathcal{D}, \quad (1)$$

where

$$\zeta = \nabla^2 \psi \quad \text{and} \quad q = \delta_I^2 \zeta + y \quad (2)$$

are the relative and potential vorticities.

The dimensionless parameters in the problem are

$$\delta_I = \left(\frac{\pi \tau_0}{\rho H \beta^2 L^3} \right)^{1/2}, \qquad \delta_s = \frac{f}{H} \left(\frac{A_v}{2f} \right)^{1/2} \frac{1}{\beta L},$$

and

$$\delta_H = \left(\frac{A_H}{\beta L^5} \right)^{1/5}, \quad (3)$$

the inertial, Stommel, and diffusive layer thicknesses scaled by the width of the basin L. The scales that lead to the nondimensional parameters and that must be used to reconstruct the dimensional variables are the following:

$$\psi_{\text{dim}} = \frac{\pi \tau_0}{\rho \beta H} \psi, \qquad t_{\text{dim}} = (\beta L)^{-1} t,$$

$$x_{\text{dim}} = Lx, \quad \text{and} \quad y_{\text{dim}} = Ly. \quad (4)$$

The domain of integration is a rectangular basin given by

$$\mathcal{D} = \{(x, y) \mid 0 < x < 1 \text{ and } -1 < y < 1\}. \quad (5)$$

The boundary conditions are the following:

$$\psi = 0, \quad \text{on } \partial \mathcal{D}, \quad (6)$$

$$\nabla \zeta \cdot \mathbf{n} = 0, \quad \text{on } \partial \mathcal{D}, \quad (7)$$

$$\nabla (\nabla^2 \zeta) \cdot \mathbf{n} = 0 \quad \text{on } \partial \mathcal{D}. \quad (8)$$

Note that the integral of the lateral diffusive term over the entire basin vanishes because of the no-flux boundary conditions in Eq. (8), so that no net source or sink of vorticity is introduced by the lateral diffusion. The source of vorticity due to the curl of the wind stress is given by

$$\nabla \times \tau = \pi \sin(\pi y). \quad (9)$$

As Veronis (1966) discusses, the fact that many com-

plicating physical processes are assumed out of the system means that we cannot think of such a simple model as the first term in a sequence that converges to the ''real'' ocean. Rather, the utility of such a model is that it can be used to check and build our intuition about the behavior of oceanic models. In this respect, it is better thought of as being at the base of a hierarchy of models that have successive levels of sophistication and realism. Investigating the behavior of the model as parameters are allowed to tend to various limits is fundamental in characterizing its behavior. Thus, the goal of this study is to consider a wide range of parameter $(\delta_I, \delta_S, \delta_H)$ values.

It is useful to consider some typical values for the model's parameters that give results reproducing the major gross featurs of the wind-driven circulation. Following Marshall (1984), the inertial layer thickness $\delta_I = \sqrt{1 \times 10^{-3}} = 0.0316$ corresponds to an ocean in which $\tau = 10^{-1}$ N m^{-2}, $\rho = 10^3$ kg m^{-3}, $\beta = 2 \times 10^{-11}$ m^{-1} s^{-1}, $H = 5 \times 10^2$ m, and $L = 10^6$ m; the nondimensional Stommel layer thickness $\delta_S = 10^{-2}$ corresponds to $f = 10^{-4}$ s^{-1}, $A_v = 1 \times 10^{-4}$ m^2 s^{-1}, and the horizontal hyperdiffusive thickness $\delta_H = 0.0313$ corresponds to $A_H = 6 \times 10^{11}$ m^2 s^{-1}. The timescale is given by $T = 1/\beta L$ so that one can relate δ_S to a damping timescale of $\sigma = 1/(\delta_S \beta L) = 58$ days. The lateral diffusion parameter is usually chosen to be the smallest possible value that will keep the vorticity fields free of grid-scale oscillations. It is often justified as an effective eddy viscosity. Eddy viscosities are difficult to estimate from observations. Many physical processes contribute to the effective dissipation. Most of these processes cannot be directly simulated in a barotropic QG model and are lumped in the effective eddy diffusivity, while others like the internal compensation mechanism, can be simulated provided the model resolution is sufficient to allow eddies. The model behavior is relevant even where it does not produce realistic flows, since it helps to understand how processes that are being simulated depend on those processes parameterized by eddy diffusivity. The method of solution is discussed in detail in appendix A.

3. Multiple equilibria

a. Bifurcation structure as a function of δ_I and δ_S

Using a continuation algorithm for finding both steady-state solutions and the corresponding least stable eigenmode (or one of the unstable eigenmodes if the solution is unstable), the bifurcations of the steady-state equilibria were mapped as a function of the nondimensional parameters δ_I and δ_S. All of the solutions presented in this section used $N_x = 33$ and $N_y = 65$ grid points in the x and y directions, respectively, with uniform grid spacing of $dx = dy = 0.03$. The lateral diffusivity was fixed at $\delta_H = 0.04$, which is slightly larger

than the grid spacing. Section 3g discusses the sensitivity of the solutions to the magnitude of δ_H.

For parameter values in the range $0.01 < \delta_S < 0.1$ and $0 < \delta_I \leq 0.4$, up to six different types of equilibria were found. Each will be discussed in turn in the next subsections. Before proceeding it is useful to give a review of the multiple equilibria results of Cessi and Ierley (1995) followed by a brief overview of the multiple equilibria found in this study.

It is important to recall that the model formulation used by Cessi and Ierley, as well as the one used here, satisfies the symmetry property $\psi \rightarrow -\psi$, $y \rightarrow -y$. Equilibrium states that satisfy the above symmetry property are said to be antisymmetric and those that do not are said to be nonsymmetric. Because of this symmetry property, nonsymmetric equilibria always come in pairs that are related to each other by $\psi \rightarrow -\psi$, $y \rightarrow -y$. Cessi and Ierley (1995), identified five different types of equilibria in a parameter space defined by (δ_I, δ_M), where δ_M is the nondimensional Munk boundary layer thickness. Their multiple equilibria included three different antisymmetric equilibria, which they called type A1, A2, and A3, as well as two pairs of nonsymmetric equilibria, which they called type N1 and N2.

For the entire region of parameter space explored in the present study, only one antisymmetric equilibrium was found. In the terminology of Cessi and Ierley, this equilibrium solution is said to be of type A. Other regions of parameter space have alternate equilibria that come into existence via bifurcations of this antisymmetric equilibrium. These equilibria are nonsymmetric and come in pairs. Three types of nonsymmetric equilibria bifurcate from the antisymmetric equilibrium, those of type N1 and N2, as well as a third not found by Cessi and Ierley, which we define to be of type N3. Finally, the solution branch of type N1 undergoes a fold catastrophe, whereby two additional nonsymmetric equilibria come into existence. We call these type N1$_1$ and N1$_2$. Each of these solution types are discussed in the following subsections.

b. Antisymmetric equilibria (type A)

In Fig. 1, a parameter plot indicates the bifurcations of the antisymmetric equilibria, discussed below. Typical antisymmetric streamfunction and potential vorticity fields are shown in Fig. 2. This sequence of antisymmetric equilibria is taken along the left-most side of the parameter plot shown in Fig. 1. Apart from being antisymmetric, these equilibrium solutions are characterized by the formation of inertial recirculation cells flanking the southern and northern edge of the intergyre boundary. It is important to mention that the formation of closed recirculation cells trapped near the western wall does not occur when δ_S is bigger than δ_H. This point will be further discussed in section 3g. The remainder of this section is restricted to the case $\delta_H > \delta_S$.
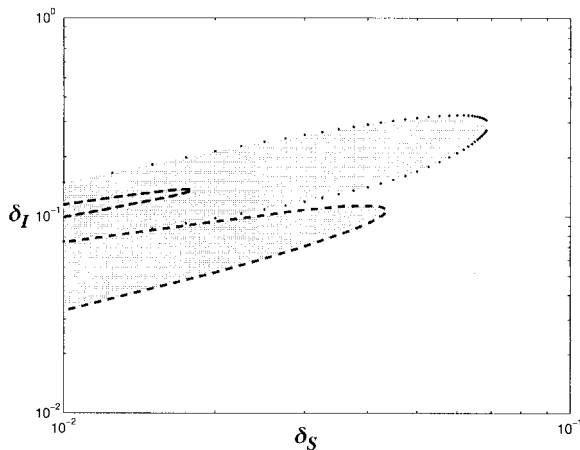
FIG. 1. Parameter plot for $\delta_H = 0.04$ showing the bifurcations of the antisymmetric equilibrium (type A). Dashed lines indicate pitchfork bifurcations and dotted lines indicate Hopf bifurcations. The antisymmetric equilibrium exists for the full range of parameters shown in the plot. It is unstable in the shaded region and stable elsewhere. The lower dashed lobe, indicates where nonsymmetric equilibria of type N1 (lower part of lower dashed lobe) and of type N2 (upper part of lower dashed lobe) bifurcate from the antisymmetric equilibrium via a symmetry-breaking pitchfork bifurcation. The upper dashed lobe indicates where nonsymmetric equilibria of type N3 bifurcate from the antisymmetric branch via a pitchfork bifurcation.

For moderate values of δ_I, the recirculation cells are small and trapped near the western wall (Fig. 2, $\delta_I = 0.03$). In the region of parameter space near the first pitchfork bifurcation (lower part of the lower dashed lobe in Fig. 1), both viscous effects and advection of planetary and relative vorticity are important near the western boundary layer and in the region near the recirculation gyres. Note how the q contours run almost parallel to the western wall and form a sharp front where the latitude of zero wind stress curl intersects the western boundary. Away from the western boundary and recirculation cells, the flow is essentially in Sverdrup balance. In this region, the q contours are now parallel to the latitude lines. For increasing values of δ_I, the recirculation cells expand in size, in both the zonal and meridional directions. For parameter values close to the second pitchfork bifurcation (upper part of the lower dashed lobe in Fig. 1), the recirculation gyres have expanded across the basin to the eastern wall (Fig. 2, $\delta_I = 0.06$). Further increasing δ_I leads to basin-filling inertial gyres (Fig. 2, $\delta_I = 0.12$). Note how the q or ζ contours are parallel to the streamlines. The Sverdrup balance is then no longer valid anywhere in the basin. The dominant balance is quasi inertial, that is, $J(\psi, \nabla^2\psi) \sim 0$. Bottom friction, which is not important in any local balance, is nevertheless important in maintaining the gyre-integrated vorticity balance.

The lower dashed lobe in Fig. 1 is the location of bifurcation points at which nonsymmetric equilibria of type N1 and N2 bifurcate from the antisymmetric equilibrium. The lower part of the dashed curve gives rise to fixed points of type N1 and the upper part gives rise to fixed points of type N2. The nonsymmetric equilibrium of type N1 and N2 will be described in subsections 3c and 3d, respectively. The upper-dashed lobe inside the dotted lobe in Fig. 1 is the location of bifurcation points leading to nonsymmetric equilibria of type N3. Equilibria of type N3 are described in section 3e. Figure 3, which is fully discussed in section 4, shows a bifurcation plot of $\max\psi + \min\psi$ (a measure of the assymetry of the solution) versus δ_I for a value of $\delta_S = 0.01$, which is along the left-most side of the parameter plot shown in Fig. 1. It shows the four symmetry breaking pitchfork bifurcations that occur as one moves upward and accross the dashed lobes in Fig. 1.

The antisymmetric equilibrium is unstable for parameter values in the shaded regions of Fig. 1 and stable in the unshaded region. The marginal stability curve separating stable from unstable regions of parameter space is composed of a curve along which Hopf bifurcations occur (dotted line) and a curve along which pitchfork bifurcations occur (lower dashed lobe). Hopf bifurcations lead to self-sustained oscillations of the flow field, and pitchfork bifurcations are at the origin of symmetry-breaking multiple equilibria.

c. Nonsymmetric equilibrium (type N1)

In Fig. 4, a parameter plot indicates the bifurcations associated with the nonsymmetric equilibrium state of type N1. Typical nonsymmetric streamfunction and potential vorticity fields of type N1 are shown in Fig. 5, along with equilibria of type A and N2 for comparison. As mentioned above, the nonsymmetric states of type N1 come into existence via a symmetry breaking pitchfork bifurcation of the antisymmetric state. The pitchfork bifurcation points that mark the emergence of the type N1 equilibria are located on the lower dashed curve in Fig. 4. The nonsymmetric equilibria exist only in the region bounded by the lower dashed curve, and the upper solid curve. Within this region, it is stable in the unshaded area and unstable in the shaded area. Within the wedge-shaped region bounded by the saddle node bifurcations emanating from the cusp point labeled CP1, there are two additional equilibria defined to be of type $N1_1$ and $N1_2$. The distinction between equilibria of types N1, $N1_1$, and $N1_2$ is essentially in the geometrical arrangement of the multiple circulation cells within the basin. A full discussion of equilibria of type $N1_1$ and $N1_2$ will be given in section 3f. Along the solid curve labeled SN1, the N1 branch experiences a saddle-node bifurcation and nonsymmetric equilibria of type $N1_1$ come into existence. The equilibria of type $N1_1$ also experience a saddle-node bifurcation along the lower solid curve labeled SN2, and nonsymmetric equilibria of type $N1_2$ come into existence. Referring again to Fig. 3, one can see the saddle-node bifurcations as one moves across the solid curves in Fig. 4.

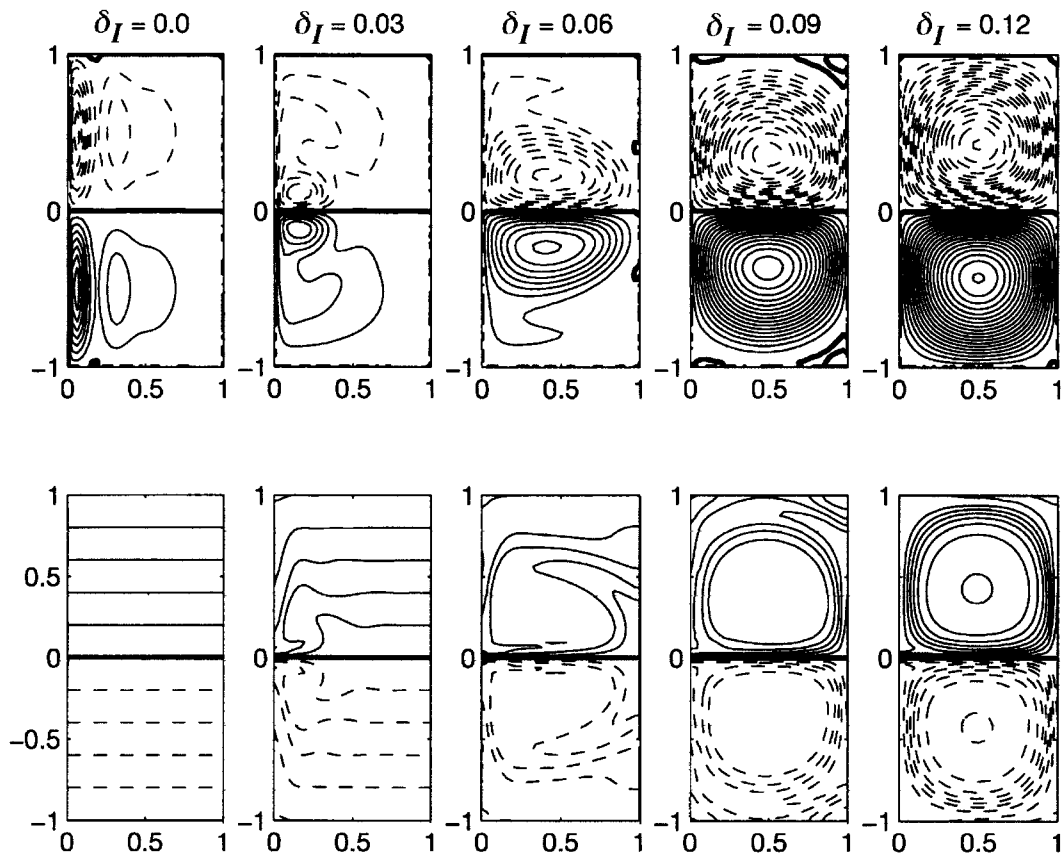In the neighborhood of the pitchfork bifurcation point

FIG. 2. Contour plots of ψ (top row) and q (bottom row) for the antisymmetric equilibrium (type A) with $\delta_S = 0.01$, $\delta_H = 0.04$, and δ_I as indicated. The dashed lines indicate the negative contours and the solid lines indicate the positive contours. The thick solid line indicates the zero contour. The contour interval is 0.03 for ψ and 0.02 for q.
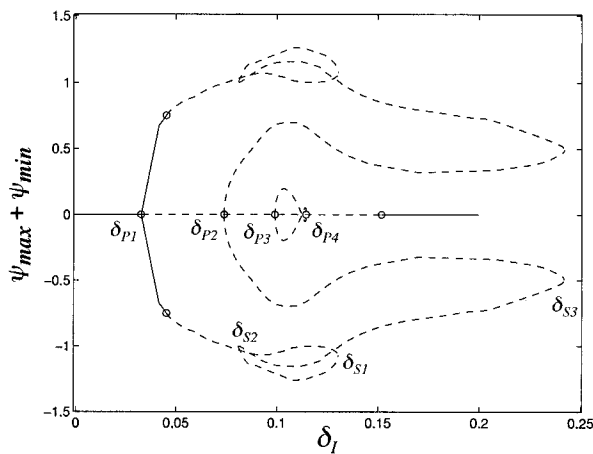

FIG. 3. Bifurcation plot of $\psi_{max} + \psi_{min}$ vs δ_I, indicating the emergence of nonsymmetric equilibria N1 and N2 and N3 via pitchfork bifurcations at $\delta_I = \delta_{P1}$, δ_{P2}, and δ_{P3}. A fourth pitchfork bifurcation point at $\delta_I = \delta_{P4}$ marks the disappearance of the nonsymmetric equilibria of type N3. Antisymmetric equilibria lie on the horizontal line in the center of the figure. Saddle-node bifurcation points at $\delta_I = \delta_{S1}$, δ_{S2}, and δ_{S3} mark the merging of equilibria of types N1 with N1$_1$, N1$_1$ with N1$_2$, and N1$_2$ with N2. The solid curves indicate stable equilibria and the dashed lines indicate unstable equilibria ($\delta_S = 0.01$, $\delta_H = 0.04$).
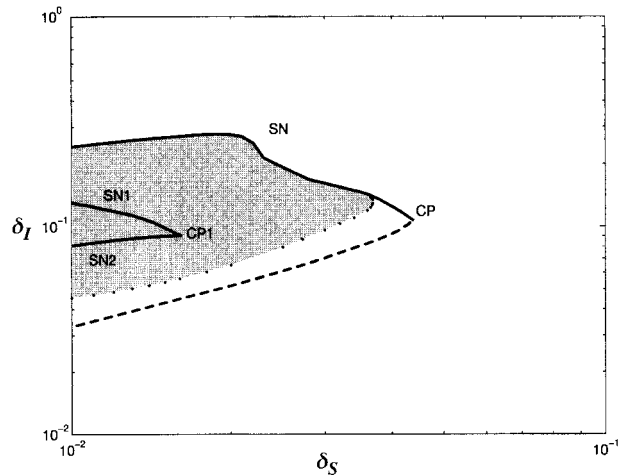
FIG. 4. Parameter plot for $\delta_H = 0.04$ showing the bifurcations of the nonsymmetric equilibria of type N1. Solid lines denote saddle-node bifurcations, dashed lines indicate pitchfork bifurcations, and dotted lines indicate Hopf bifurcations. Equilibria of type N1 can be traced continuously for increasing values of δ_I from the dashed curve (where they bifurcate from the antisymmetric equilibrium) up to the saddle-node curve labeled SN or SN1 depending on whether δ_S is to the right or left of the cusp point labeled CP1.
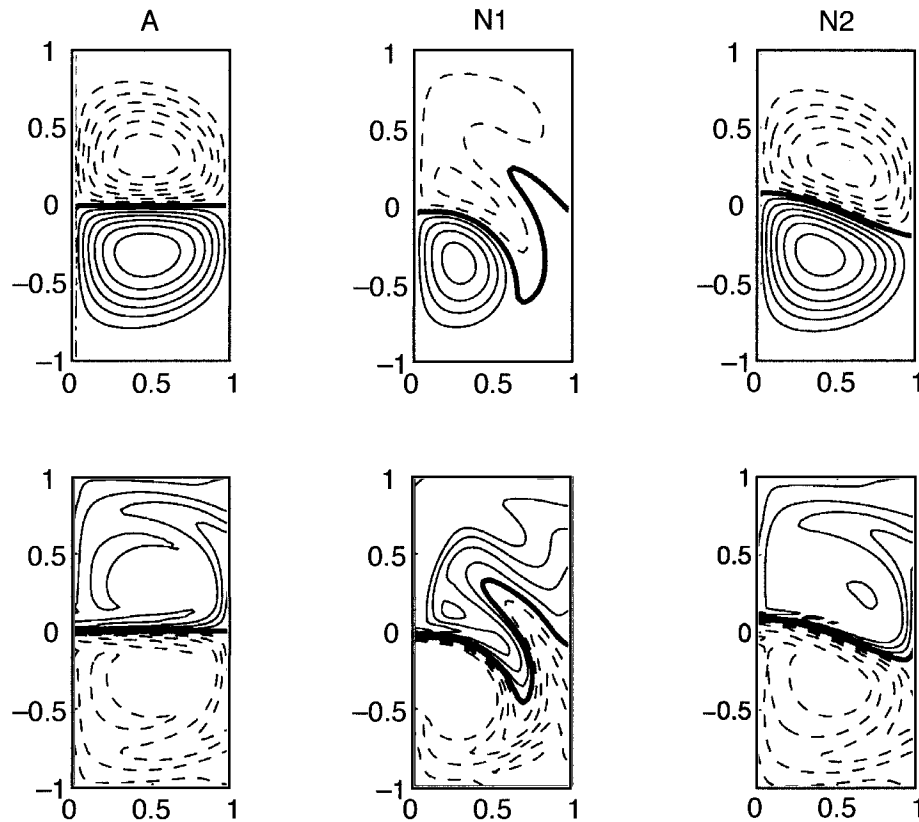
FIG. 5. Typical ψ and q fields for the branches A, N1, and N2: $\delta_I = 0.1001$, $\delta_S = 0.02$, and $\delta_H = 0.04$. The contour interval is 0.3 for ψ and 0.2 for q. Negative contours are dashed, and the zero contour is the thick one.

the equilibria are characterized by moderate recirculation gyres with essentially the same vorticity balance as the antisymmetric state, provided that $\delta_H > \delta_S$ (see discussion in section 3g). As δ_I is increased, and one moves away from the bifurcation point, one of the recirculation cells becomes stronger. The weaker of the two recirculation cells crosses the line of zero wind stress curl as it is pulled by its more intense counterpart. As δ_S is decreased, and δ_I is kept near the center of the shaded region in Fig. 4, the flow field becomes progressively more asymmetric, with large meanders crossing the latitude of zero wind stress curl. These meanders permit vorticity to be fluxed across the latitude of zero wind stress curl so that the integrated vorticity balance need not be achieved entirely by bottom friction. This allows equilibria of type N1 to remain of much weaker intensity than its antisymmetric counterpart of type A, as δ_I is increased. Equilibria of type A, N1, and N2 can be compared in Fig. 5. One should note in particular how the nonsymmetric equilibrium of type N1 are somewhat intensified in the western part of the basin and much weaker than those of type A or N2. A further and more dramatic example of the different vorticity balance achieved by nonsymmetric equilibria of type N1 can be observed in Fig. 6 by comparing equilibria of type A,

N1, and N2. The multiple equilibria in this figure were computed for the same parameter values as those used in the time-dependent simulation of Marshall (1984) ($\delta_S = 0.001$, $\delta_H = 0.0313$, and $\delta_I = 0.0316$). The streamfunction field labeled PBAR in Fig. 6 is the time average of a simulation of the time-dependent flow field. The equilibria of type N1 are unstable in this region of parameter space. The time-dependent flow field evolved in a complicated way with many strong eddies forming. Nevertheless, the integrated vorticity balance over the region of negative wind stress curl is similar to that of time-averaged flow, provided the role of the eddy-induced vorticity flux in the time-dependent case is replaced by the flux of vorticity across the line of zero wind stress curl by stationary meanders in the steady case. In the steady-state solution, bottom friction removed only 4% of the vorticity input by the wind and in the time-mean state, bottom friction removed about 5% of the vorticity input by the wind. Furthermore, the pair of fixed points of type N1 are qualitatively similar to a typical instantaneous flow field of the time-dependent simulation.

For $\delta_S > 0.0161$ the nonsymmetric equilibrium of type N1 can be traced continuously up to a saddle-node bifurcation curve (labeled SN in Fig. 4), where it merges
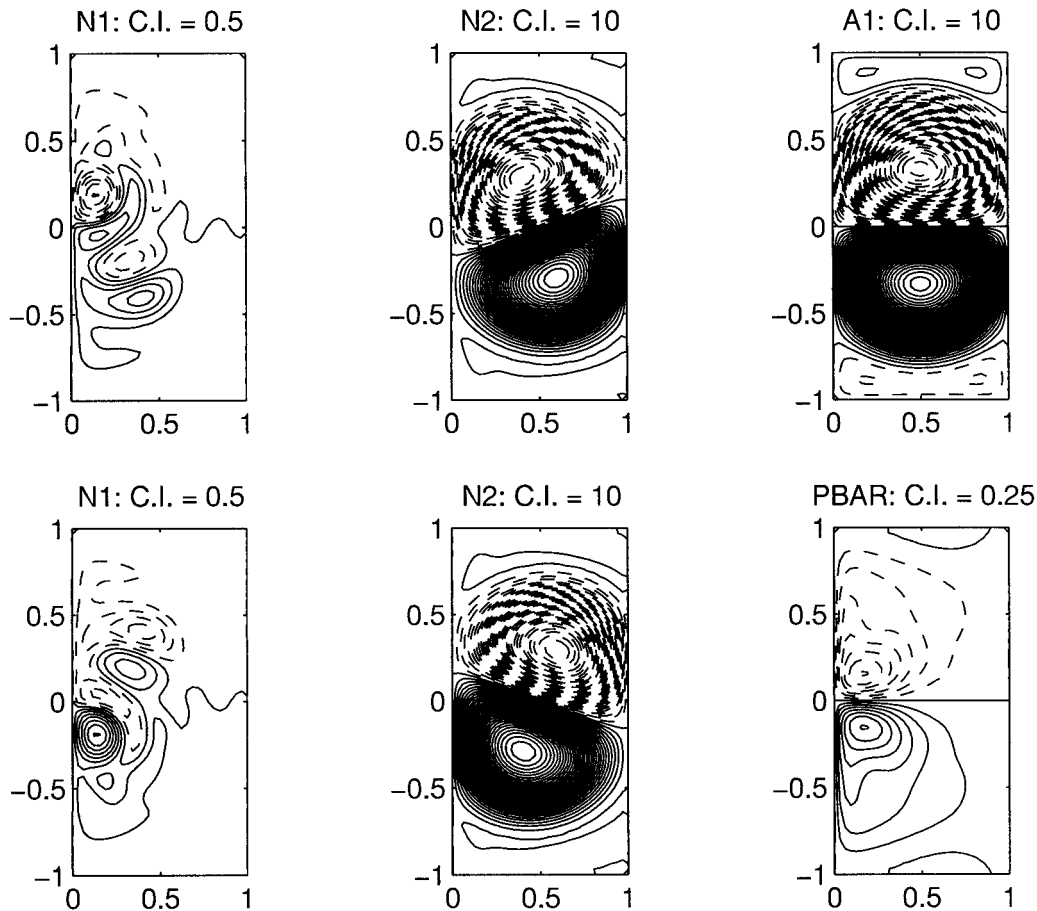
FIG. 6. Contour plots of ψ for $\delta_I = 0.0316$, $\delta_S = 0.001$, and $\delta_H = 0.0313$. Steady states of types A, N1, and N2 are presented along with the time-averaged streamfunction field (PBAR). The solid lines denote positive contours and the dashed lines denote negative contours. Contour intervals are as indicated.

with a fixed point of type N2 and ceases to exist. At δ_S = 0.0161 and δ_I = 0.090, a fold catastrophe occurs (labeled CP1 in Fig. 4), which leads to a wedge with two additional equilibrium states called type N1$_1$ and N1$_2$. These additional equilibria will be described in section 3f. Furthermore, for δ_S < 0.0161, that is, for values of δ_S to the left CP1, it is N1$_2$ that merges with N2 at SN.

d. Nonsymmetric equilibrium (type N2)

In Fig. 7, a parameter plot indicates the bifurcations associated with the nonsymmetric equilibrium state of type N2. Typical nonsymmetric streamfunction and potential vorticity fields of type N2 were shown in Fig. 5. As mentioned in section 3c, nonsymmetric equilibria of type N2 come into existence via a pitchfork bifurcation of the antisymmetric equilibrium. This pitchfork bifurcation has its origin at the cusp point labeled CP in Fig. 7. Equilibria of type N2 are always unstable. This branch can be traced continuously up to a saddle-node bifurcation point lying on the solid curve where it merges

with the equilibrium of type N1 and disappears. The pitchfork bifurcation and the saddle-node bifurcation can be seen in Fig. 3 for δ_S = 0.01.

Near the cusp point in Fig. 7, there is little difference between equilibria of types N1 and N2. In this region of parameter space a three-term balance is achieved between the advection of planetary vorticity, advection of relative vorticity, and lateral diffusion. However, the vorticity balance integrated over the region of either positive or negative wind stress curl is achieved primarily by bottom friction. As δ_S is decreased and δ_I is kept in the center of the shaded region in Fig. 7, the equilibria of type N1 and N2 separate themselves through different balances. The nonsymmetric equilibrium of type N2 is characterized by inertial gyres ($J(\psi, \nabla^2\psi) \sim 0$) that extend across the basin. Again, the bottom friction term is unimportant in any local balance but is nonetheless crucial in maintaining the global vorticity balance. This should be contrasted with nonsymmetric equilibria of type N1, where viscous effects are important locally in the region near the western wall,
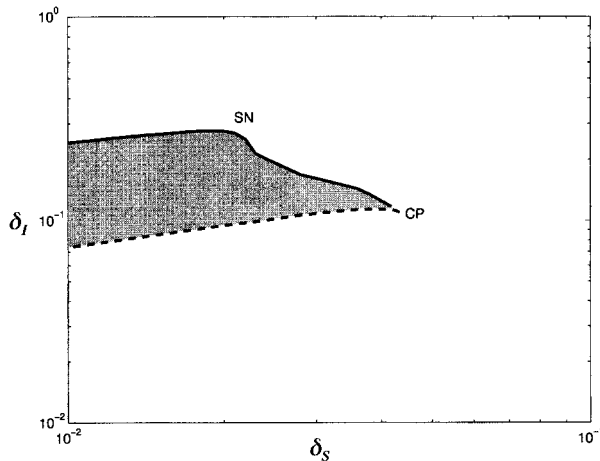
FIG. 7. Parameter plot for $\delta_H = 0.04$ showing the bifurcations of the nonsymmetric equilibrium (N2). Solid lines denote saddle-node bifurcations and dashed lines indicate pitchfork bifurcations. Equilibria of type N2 exist only in the shaded region of parameter space where it is also always unstable. Nonsymmetric equilibria of type N2 come into existence via a pitchfork bifurcation of the antisymmetric flow and can be traced continuously as as δ_I is increased up to the solid curve labeled SN where it experiences a saddle-node bifurcation, merges with equilibria of type N1, and ceases to exist.

and where the intergyre boundary meets the western wall.

e. Nonsymmetric equilibrium (type N3)

Nonsymmetric equilibria of type N3 exist inside the region bounded by the upper dashed lobe of Fig. 1. Typical ψ and q fields for the nonsymmetric equilibria of type N3 and, for comparison, antisymmetric equilibria are presented in Fig. 8. Nonsymmetric equilibria of type N3 come into existence via a pitchfork bifurcation of the antisymmetric equilibrium. The equilibrium is characterized by basin-filling inertial gyres with the intergyre boundary shifted either north or south and tilted in the east–west direction. Both equilibria of types A and N3 are characterized by a quasi-inertial balance; the difference in the solution is restricted to their different symmetry properties.

f. Nonsymmetric equilibria (types N1$_1$ and N1$_2$)

Nonsymmetric equilibria of type N1$_1$ and N1$_2$ come into existence via a fold catastrophe of the solution branch of type N1. In Fig. 4, the region of parameter space where this fold takes place is denoted by the wedged-shaped region emanating from the cusp point labeled CP1. Figure 9 shows typical contour plots of ψ and q. These equilibria are characterized by strongly nonsymmetric flow fields, with multiple circulation cells. The essential difference between equilibria of type N1, N1$_1$, and N1$_2$ is characterized by the geometrical arrangement of circulation cells within the basin. The integrated vorticity balance for the region of either pos-
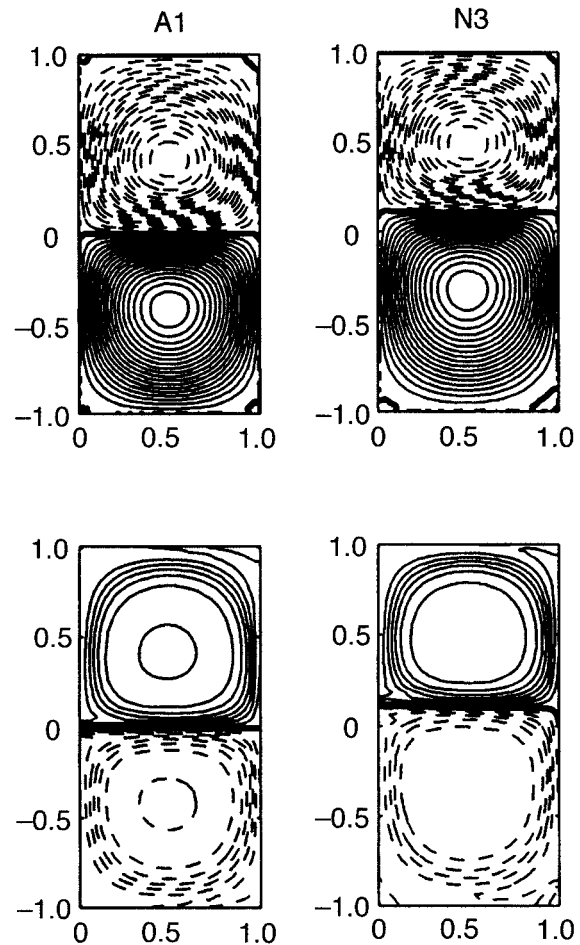

FIG. 8. Typical ψ and q fields for the branches A1 and N3: $\delta_I = 0.1127$, $\delta_S = 0.01$, and $\delta_H = 0.04$. The contour interval is 0.4 for ψ and 0.3 for q. The negative contours are dashed, and the zero contour is the thick one. The nonsymmetric branch N3 has its intergyre boundary shifted northward and tilted from west to east.

itive or negative wind stress curl is achieved primarily by stationary meanders transporting vorticity across the latitude of zero wind stress curl.

g. Dependence on lateral diffusivity parameter, δ_H

In this section, the role of the lateral diffusion parameter δ_H in modifying the model's fixed points is explored. It is interesting to compare two sequences of antisymmetric equilibrium solutions with alternate orderings of lateral friction and bottom friction layer thicknesses, that is, $\delta_H > \delta_S$ and $\delta_S > \delta_H$. In this section, computations with $\delta_H = 0.01$ were performed with $N_x = 33$ and $N_y = 129$, grid points on a grid stretched in the y direction with with $m_y = 0.25$. See appendix A for a definition of m_x and m_y. The grid spacing in the x direction was uniform $dx = 0.03$, and in the y direction the grid spacing varied from a maximum of $dy = 0.03$, near the northern and southern basin walls, and a min-
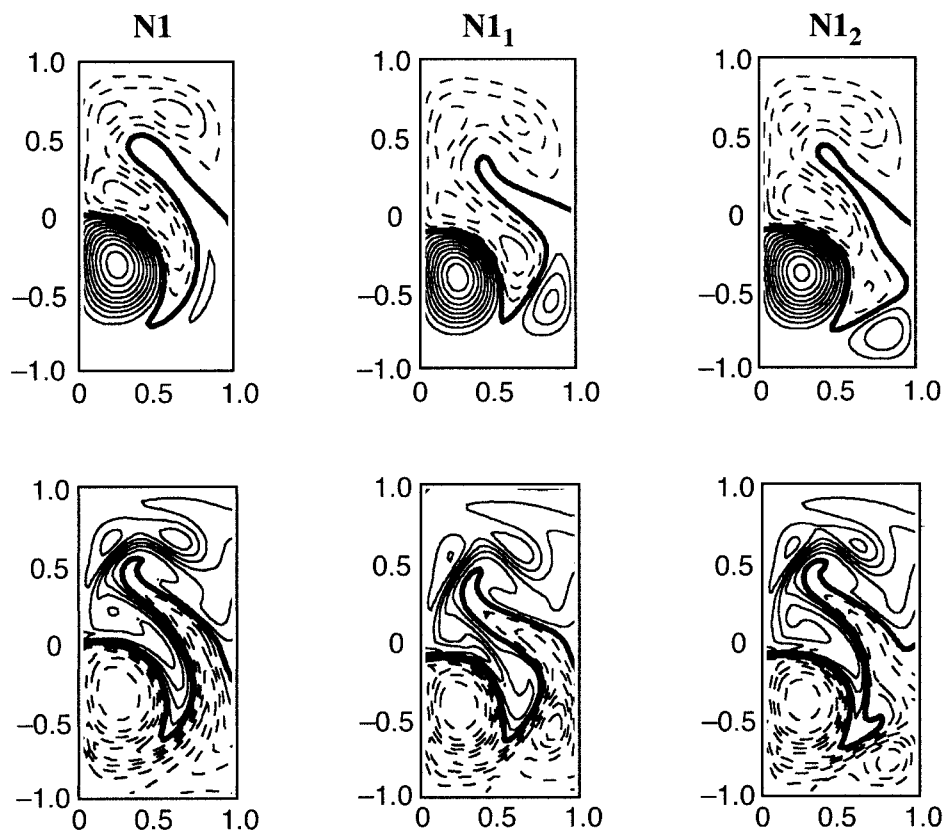
FIG. 9. Typical ψ and q fields for the branches N1, N1$_1$, and N1$_2$ for $\delta_I = 0.1$, $\delta_S = 0.02$, and $\delta_H = 0.04$. The contour interval is 0.2 for ψ and 0.2 for q. The negative contours are dashed, and the zero contour is the thick one. The difference between the three equilibrium branches is essentially restricted to the spatial arrangement of the multiple closed circulation cells.

imum of $dy = 0.0031$, near the line of zero wind stress curl. The higher resolution and stretched grid are necessary to resolve the sharp gradient in the relative vorticity field that forms where the intergyre boundary meets the western wall.

Figure 2 shows a sequence of antisymmetric equilibria for increasing values of δ_I with $\delta_H = 0.04 > \delta_S = 0.01$ fixed. For this ordering of the friction parameters, the sequence of streamfunction fields is similar to that computed by Ierley and Sheremet for the single-gyre case with Munk-type lateral diffusion. Closed recirculation cells form near the western wall where the counterrotating gyres meet. The cells expand in size and strength as δ_I is increased, eventually filling the entire basin.

Contrast this with Fig. 10, which shows a similar sequence but with the alternate ordering in the thickness of the lateral and bottom friction layers, $\delta_H = 0.01 < \delta_S = 0.04$. In this case, the sequence of equilibria is similar to the sequence of solutions computed by Veronis (1966). The jet separating the northern gyre from the southern gyre increases in strength and penetrates progressively deeper into the interior as δ_I increases.

The circulation pattern does not develop closed recirculation cells trapped near the western wall. The limit $\delta_I \to \infty$ has basin-filling gyres similar to those for the case with $\delta_H > \delta_S$, in the sense that they both have q versus ψ scatterplots with negative slope. For the case of $\delta_S > \delta_H$, there are, however, intermediate values of δ_I for which the scatterplot of q versus ψ has positive slope.

Finally, in comparing the single-gyre calculations of Veronis (1966) to the double-gyre calculations presented here, one should highlight the importance of the boundary condition experienced by the northern flank of the subtropical gyre. For a single-gyre calculation, there can be no flux of vorticity across the northern wall, which is not the case for the double-gyre calculations. This difference in boundary condition allows the northern jet to penetrate clear across the basin for either ordering of δ_H or δ_S. Tight recirculation cells trapped in the northwestern corner of the subtropical gyre can form only if $\delta_H > \delta_S$ and anomalously high potential vorticity is allowed to diffuse from the subpolar gyre into the subtropical gyre. To demonstrate this, Fig. 11 shows contour plots of the q and ψ field for a single-gyre calcu-
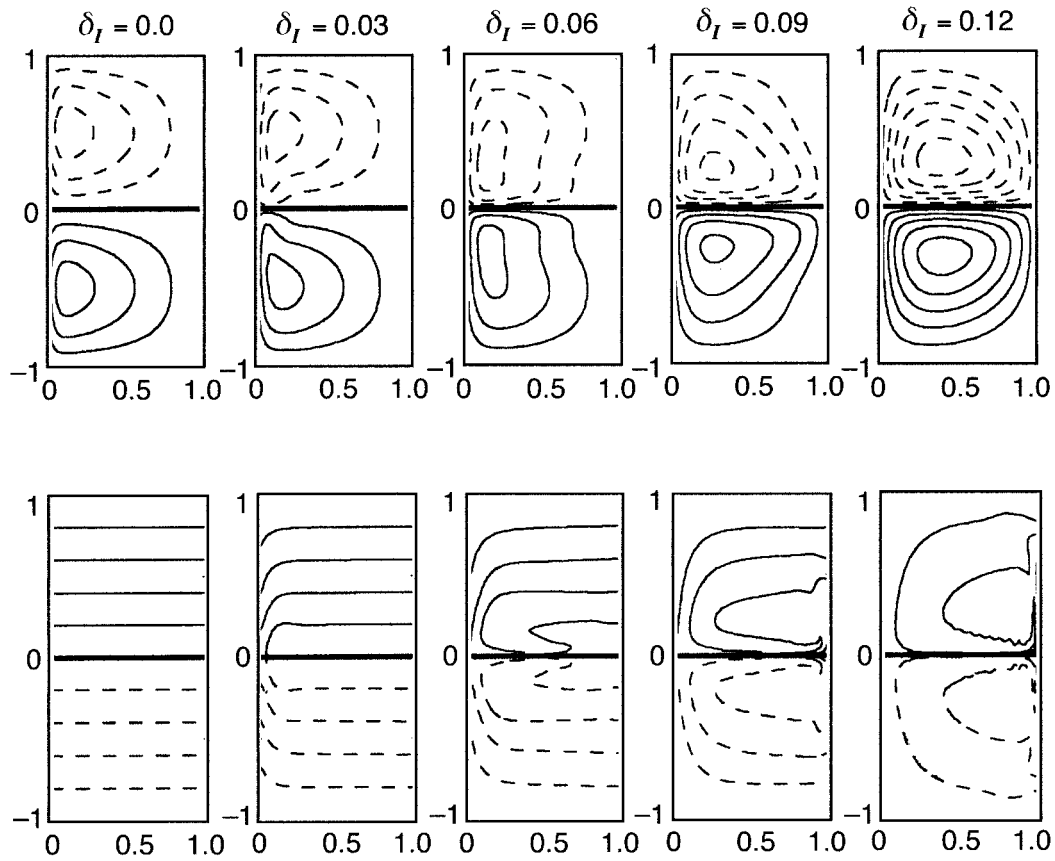
FIG. 10. Contour plots of ψ (top row) and q (bottom row) for the antisymmetric equilibrium (type A) with $\delta_S =$ 0.04 and $\delta_H = 0.01$ and δ_I as indicated. The dashed lines indicate the negative contours and the solid lines indicate the positive contours. The thick solid line indicates the zero contour. Here, C.I. = 0.02 for ψ and for q.
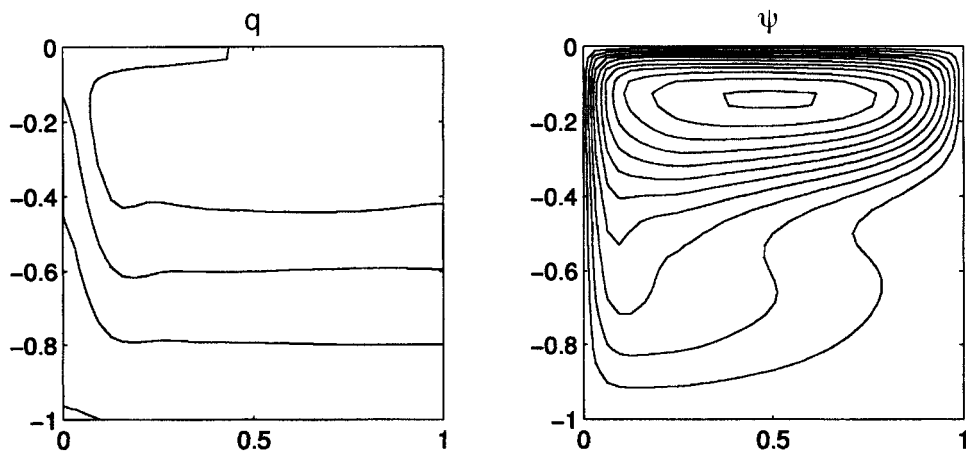

FIG. 11. Contour plots of ψ and q for the single-gyre case. The no-flux of vorticity across the northern wall allows the northern jet to penetrate straight across the basin. This should be compared with the double-gyre antisymmetric equilibria computed for the same parameters (Fig. 2, $\delta_I = 0.03$). Here, $\delta_S = 0.01$ and $\delta_H = 0.04$ and $\delta_I = 0.03$. Also, C.I. = 0.02 for ψ and C.I. = 0.02 for q.
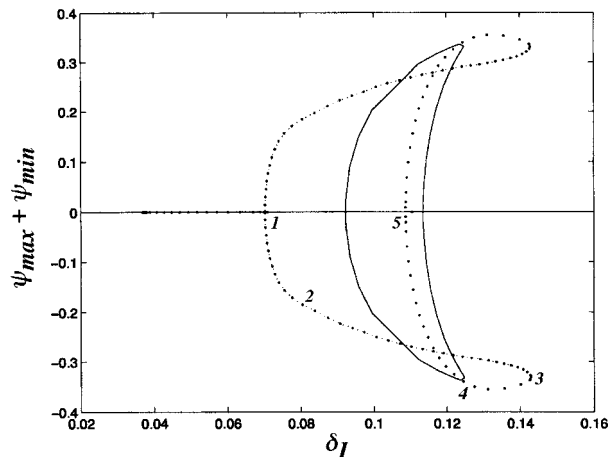
FIG. 12. Bifurcation plot of maxψ + minψ vs δ_I indicating the emergence of nonsymmetric equilibria of type N1 and N2 via pitchfork bifurcations for two different values of δ_H ($\delta_H = 0.04$ solid curve, $\delta_H = 0.01$ dotted curve), $\delta_S = 0.04$, and their disappearance at saddle-node bifurcations.

lation with $\delta_I = 0.03$, $\delta_H = 0.04$, and $\delta_S = 0.01$. This single-gyre calculation should be compared with the double-gyre steady-state equilibrium for the same parameter values (Fig. 2). Incidentally, the single-gyre model with $\delta_H = 0.04$ and $\delta_S = 0.01$ does not exhibit a saddle-node bifurcation as δ_I is increased. This is different from the results of Ierley and Sheremet (1995). It is not clear whether their bifurcation occurs for different δ_S and δ_H or if the different dissipation operator and boundary condition prevent it from occurring in the present model.

At least near the region of parameter space explored, the bifurcation structure leading to nonsymmetric equilibria of type N1 and N2 does not depend qualitatively on the value of δ_H. Figure 12 shows a plot of maxψ + minψ (a measure of asymmetry) versus δ_I, for $\delta_S = 0.04$ and δ_H set at either = 0.04 (solid line) or 0.01 (dashed line). The plot shows the emergence of nonsymmetric equilibria of types N1 and N2 as δ_I is increased. For $\delta_H = 0.01$ the pitchfork bifurcations occur for slightly smaller values of δ_I than they do for $\delta_H = 0.04$. Also for the smaller value of δ_H, the saddle-node bifurcation, where the equilibria of types N1 and N2 merge, happens at a larger value of δ_I. The top row of Fig. 13 shows contour plots of the ψ field, and the bottom row shows contour plots of the q field as one moves around the nose from point marked 1–5 in Fig. 12. The sequence begins with the antisymmetric equilibria at the location where N1 bifurcates from the antisymmetric solution (location 1); continues with a typical nonsymmetric equilibrium of type N1 (location 2), the nonsymmetric equilibrium at the nose point NP where equilibria of type N1 and N2 merge (location 3), and a nonsymmetric equilibrium of type N2 (location 4); and ends with the antisymmetric equilibrium at the point where equilibria of type N2 bifurcates from the antisymmetric branch

(location 5). Note that the tight recirculation cells that form near the western wall for the case $\delta_H > \delta_S$ are not present when $\delta_S > \delta_H$.

4. Overview of bifurcation structure

It is useful to summarize the bifurcation structures described in the previous sections. In Fig. 3, the difference in the extreme values of the magnitude of the streamfunction field in the subpolar and subtropical gyres ($\psi_{\max} + \psi_{\min}$) is plotted as a function of δ_I. This bifurcation plot is taken along the left-most edge of the parameter plots in Figs. 1, 4, and 7 and thus includes all the bifurcations described in the previous sections. It illustrates the successive symmetry-breaking bifurcations of the antisymmetric branch. The antisymmetric branch is marked by the horizontal line in the center of the plot. A pair of nonsymmetric equilibria of type N1 emerges as δ_I is increased past the first pitchfork bifurcation point at δ_{P1}. The pair of nonsymmetric equilibria of type N2 emerges as δ_I is increased past the second pitchfork bifurcation at δ_{P2}. The symmetry-breaking equilibria of type N3 emerges as δ_I is increased past the pitchfork bifurcation point at δ_{P3}. As δ_I is increased past the fourth pitchfork bifurcation point at δ_{P4}, the pair of nonsymmetric equilibria of type N3 merges with the antisymmetric branch and disappears. The plot also shows the saddle-node bifurcation point where the equilibria of type N1$_1$ and N1$_2$ are created ($\delta_I = \delta_{S1}$ and δ_{S2}), as well as the saddle-node bifurcation point ($\delta_I = \delta_{S3}$) where the equilibria of type N1$_2$ and N2 merge.

Figure 14 is a composite figure displaying an overlay of all the bifurcation curves. In each region of parameter space a pair of numerals indicates the total number of steady equilibria coexisting for the same parameter values and the number of those that are stable. For example (5, 1) would imply that there are five equilibrium states, one of which is stable. Regions with multiple stable equilibria are limited to those marked by (3, 2), where the pair of equilibria of type N1 are stable and the antisymmetric equilibrium is unstable, as well as to the region denoted by (5, 3), where the stable equilibria are of type A and N1, and the unstable equilibria are of type N2. Regions with up to 11 unstable equilibria are identified in the figure.

5. Discussion

Using a continuation algorithm for finding both steady-state solutions and their corresponding least stable eigenmode (or one unstable eigenmode if it exists), we mapped the bifurcation structure of the steady-state solutions of a barotropic wind-driven ocean model as a function of the two nondimensional parameters: the inertial layer thickness δ_I and the Stommel layer thickness δ_S. One of the goals in carrying out these calculations was to contribute to the broader objective of mapping
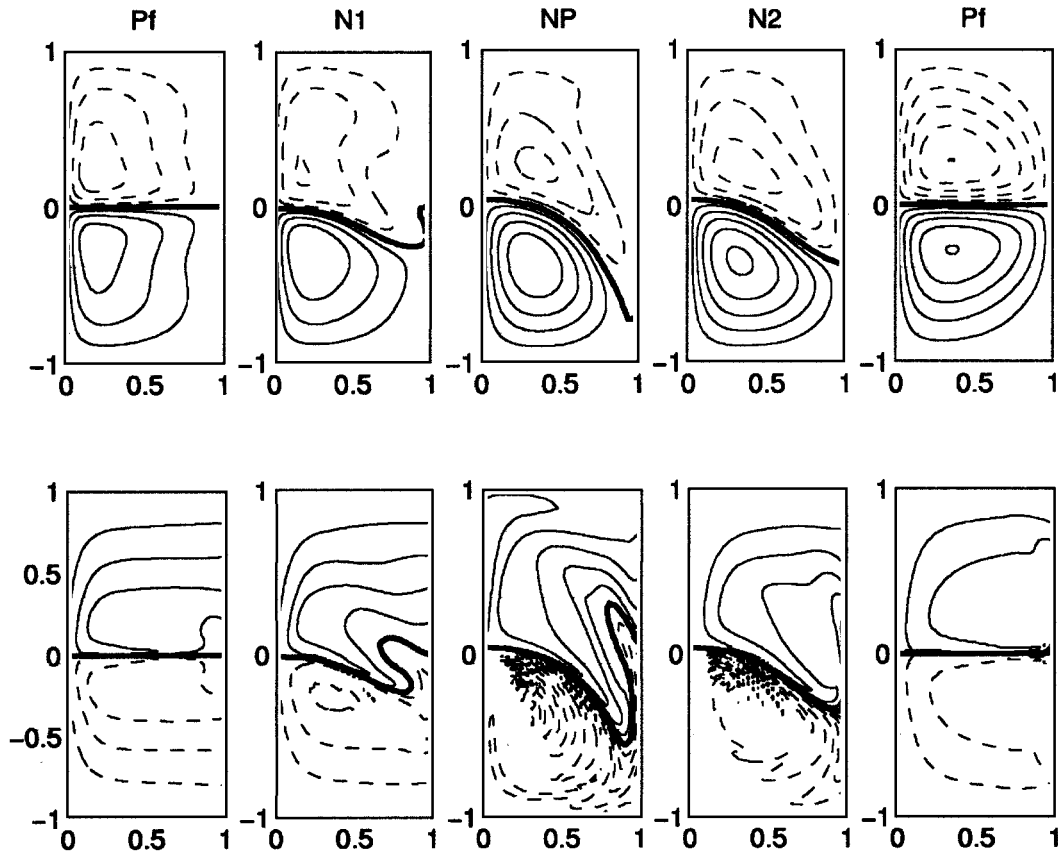
FIG. 13. Contour plots of ψ (top row) and q (bottom row) around the nose point where the branches N1 and N2 merge. The solutions correspond to values of δ_I = 0.07017, 0.08041, 0.1429, 0.1245, 0.1087, and δ_S = 0.04. The first solution labeled Pf is close to the first pitchfork bifurcation. The second solution labeled N1 is a typical solution of type N1. The third solution is close to the saddle-node bifurcation where N1 and N2 merge. The fourth solution is a typical solution of type N2, and the last solution is close to the second pitchfork bifurcation. The dashed lines indicate the negative contours and the solid lines indicate the positive contours. The thick solid line indicates the zero contour. Here, C.I. = 0.02 for ψ and C.I. = 0.02.
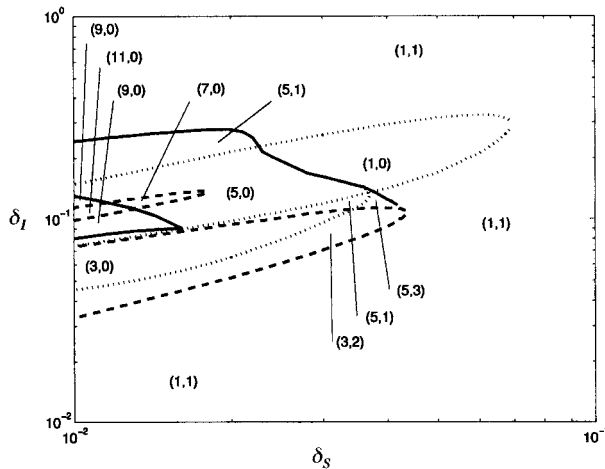

FIG. 14. Parameter plot for δ_H = 0.04 showing an overlay of the bifurcations for all the branches found. Solid lines denote saddle-node bifurcations, dashed lines indicate pitchfork bifurcations, and dotted lines indicate Hopf bifurcations.

the states of ocean models with a varying complexity of subgrid-scale parameterizations and boundary conditions. The model that we used had bottom friction and lateral diffusion with super-slip boundary conditions. In this sense this study is a continuation of the work of Cessi and Ierley (1995).

a. Inertial runaway

One solution branch (type A) can be traced continuously from the linear regime to the highly inertial regime. Like the forcing function, this branch is antisymmetric about the midbasin latitude. For sufficiently strong forcing or sufficiently weak bottom friction, the antisymmetric solution tended toward a highly inertial circulation with transports far in excess of those predicted by Sverdrup balance. Apart from having unrealistically large transports, the inertial runaway solution shows no westward intensification. Furthermore, for all values of δ_S explored, increasing δ_I eventually leads to a region where the antisymmetric steady state is stable
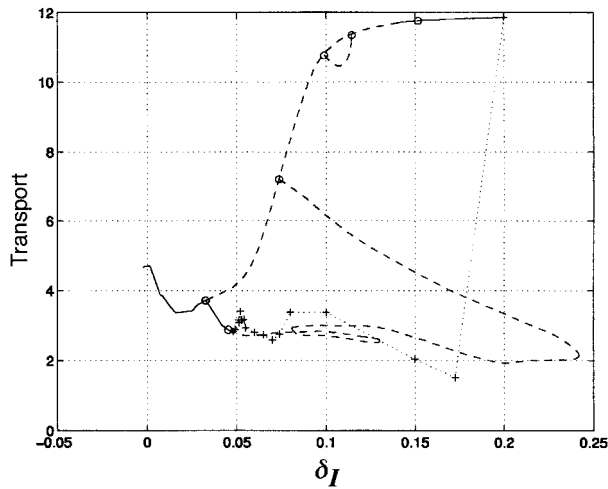
FIG. 15. Maximum transport for steady-state solution and time-averaged solutions as a function of δ_I. Dotted lines with "+" indicate time-averaged solutions. Solid lines indicate stable steady-state solutions and dashed lines indicate unstable steady-state solutions. Here, $\delta_S = 0.01$ and $\delta_H = 0.04$.

and apparently unique. A limited number of time-dependent calculations with parameters in the region labeled (1, 1) in Fig. 14 all converged to the antisymmetric fixed point, regardless of the initial conditions used, suggesting that this fixed point is a global attractor at sufficiently large values of δ_I.

The stability of the antisymmetric solution as $\delta_I \to \infty$ should be contrasted with the stability results of Cessi and Ierley for the nonlinear Munk model with free-slip boundary conditions at the eastern and western walls. They found that for $\delta_I \to \infty$ and $\delta_M \ll 1$, where δ_M is the nondimensional Munk layer thickness, the only equilibrium is *unstable* and has a single unstable eigenmode. The difference in stability between Cessi and Ierley's model and the one considered in this study can be attributed to the bottom friction term as opposed to the choice of lateral diffusion operator and boundary conditions. To verify this, some of the calculations of Cessi and Ierley were repeated with and without bottom friction. The calculations were carried out to values of δ_I as high as 300, with $\delta_S = 0$. The growth rate of the unstable eigenmode remained positive but decreased monotonically. The computations were then repeated with the addition of a bottom friction term, with a finite
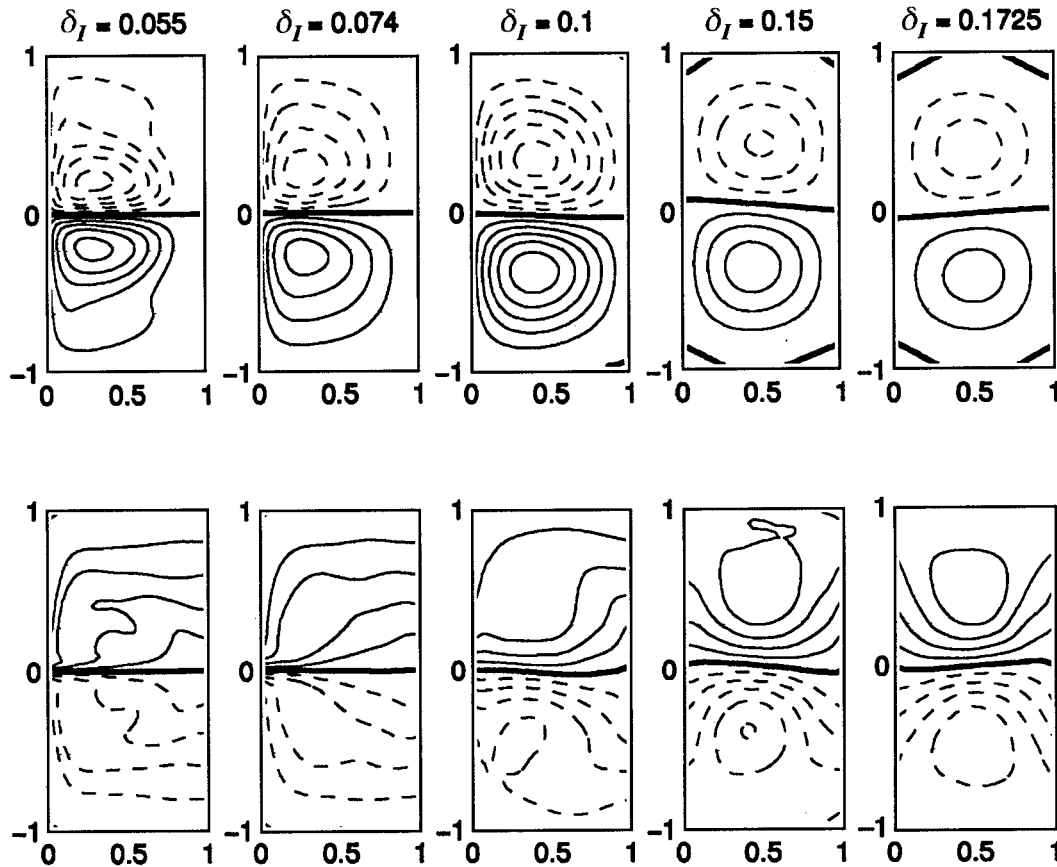

FIG. 16. Time-averaged streamfunction (top row), and potential vorticity field (bottom row) for an increasing sequence of δ_I. Other parameters are held fixed at $\delta_S = 0.01$ and $\delta_H = 0.04$.

value of δ_S, and the unstable mode became stable for a sufficiently large value of δ_I.

Another difference between our results and those of Cessi and Ierley (Cessi and Ierley 1995) is the nonexistence of a cusp catastrophe leading to multiple antisymmetric equilibria. Recall that the model used here has bottom friction, lateral diffusion in the form of a biharmonic operator acting on the vorticity, and superslip boundary conditions, which do not allow a flux of vorticity through the basin walls. We have investigated whether the choice between free-slip and superslip boundary conditions as opposed to the form of the dissipation operator could be responsible for the existence of this cusp catastrophe. Using free-slip boundary conditions ($\zeta = \nabla^2\zeta = 0$ on $\partial\mathcal{D}$) we deduced the existence of a cusp for δ_S between 0.01 and 0.001. On the other hand, for the superslip case, no cusp leading to multiple antisymmetric equilibria exists for values of bottom friction greater than $\delta_S > 0.001$. It is not clear if the cusp exists for smaller values of δ_S and δ_H or if the superslip boundary conditions truly prevents it from forming for any value of the dissipation parameters. Using a single-gyre model, Ierley and Sheremet (1995) found the cusp catastrophe when lateral diffusion and free-slip boundary conditions were used. However, they did not find the cusp catastrophe when bottom friction was used instead of lateral diffusion. A model with bottom friction alone does not allow vorticity to diffuse through the basin wall and is similar, in this sense, to a model with lateral diffusion and a super-slip boundary condition. Perhaps lateral diffusion of vorticity through the basin wall is an essential element to the dynamical balance that allows for the existence of multiple antisymmetric equilibria. Reducing bottom friction and holding lateral diffusion fixed at values of $\delta_H \geq 0.01$ does not lead to a fold of the antisymmetric branch. We have not, however, eliminated the possibility that a reduction of lateral diffusion would give rise to a fold in the antisymmetric branch.

b. Internal compensation

As was already pointed out, for high boundary-layer Reynolds number, the antisymmetric solution has a basin-filling inertial gyre with no western intensification and transports far in excess of those predicted from Sverdrup balance. As in the case of the single-gyre solutions found by Ierley and Sheremet (1995), a large eddy viscosity is needed for the model's antisymmetric solution to have western intensification and a mass transport comparable to that observed in the real ocean. Ierley and Sheremet (1995) point out that a transfer of vorticity between adjacent gyres—a mechanism that is precluded in a single-gyre model—should reduce the need for a large eddy viscosity. Indeed, in idealized double-gyre models, the intergyre transfer of vorticity can be the primary mechanism by which the wind stress curl vorticity input is balanced within each half of the basin as shown in Harrison and Holland (1981) and Marshall (1984).

For double-gyre models that have no net input of vorticity over the entire basin, there is the possibility that the vorticity balance can be achieved internally without the need for vorticity to be fluxed through the basin walls or bottom. Cessi and Ierley (1995) have demonstrated that double-gyre models with antisymmetric wind stress curl profile admit nonsymmetric solutions. We also found symmetry-breaking pitchfork bifurcations leading to nonsymmetric equilibria (types N1, N2, N3). Because of their nonsymmetry with respect to the wind forcing, these solutions have currents that transport vorticity across the latitude of zero wind stress curl. For these nonsymmetric solution, the input of vorticity by the wind stress curl in each half of the basin is balanced in part by the export of vorticity by the current. This additional mechanism for removing vorticity lessens the burden on the explicit dissipation for balancing the vorticity budget. Consequently these solutions have weaker currents than the antisymmetric solution. Figure 15 shows a plot of the difference between the maximum and minimum of the streamfunction, a quantity proportional to the maximum transport in the basin, as a function of δ_I. The solid curves correspond to equilibria that are stable and the dashed lines correspond to equilibria that are unstable. The crosses connected by the dotted line correspond to a series of time-averaged solutions. The initial condition for these simulations were the steady state of type N1 plus some random noise perturbation. One can see that the transport for the antisymmetric solution (labeled A) is always higher than that of the nonsymmetric solutions (labeled N1, N2, and N3). The time-averaged solutions also show reduced transports compared to the antisymmetric steady-state solutions. In fact, the time-averaged transports are of a magnitude comparable to those of the nonsymmetric branch of type N1. It appears that unstable fixed points of type N1 are close to a more complicated attractor that includes the model trajectories for which the time-averaged solutions were computed. Whether or not these fixed points are part of this attractor remains a conjecture since we have not attempted to compute more complicated orbits like limit cycles or homoclinic and heteroclinic orbits.

The nonsymmetric equilibria only exist for a finite range of parameters between the first pitchfork bifurcation point labeled PF1 and the last turning point labeled SN. Beyond the turning point all the computed model trajectories converged to the antisymmetric inertial runaway solution. Even before the nose point is reached, some model trajectories asymptote to the stable antisymmetric branch. In the regions labeled (5,1) in Fig. 14, it is the initial condition that determines whether the model trajectory fluctuates in some complicated

manner in the neighborhood of the N1 fixed points or asymptotes to the stable equilibrium of type A, which is where, as already mentioned, all model trajectories converged for parameter values beyond SN. We can conclude from these results that inertial runaway is unavoidable as the boundary layer Reynolds number, δ_I/δ_S, becomes sufficiently large.

Intergyre fluxes of vorticity prevent the time-averaged solution from developing unrealistically large transports, but they do not necessarily restore a Sverdrup-type balance in the interior of the basin. Figure 16 shows a sequence of time-averaged streamfunction and potential vorticity fields for δ_I between 0.055 and 0.1725. The duration of the averaging period ranged from 2500 nondimensional time units to 10 000 nondimensional units. This corresponds to averaging periods of 4–16 yr using the dimensional scales given in section 2. As the forcing increases (increasing δ_I) the western intensification of the solution decreases despite the fact that the solutions do not become highly inertial. Only close to the marginal stability curve does the time-averaged solution retain some degree of western intensification.

c. Future work

Although the idealized antisymmetric wind-forcing is unrealistic, the artificial symmetry is useful because the pitchfork bifurcations allows the nonsymmetric branches to be connected to the antisymmetric branch. For a nonsymmetric model, some of the solution branches would form isolated curves in parameter space and might not be accessible using continuation methods. Once the multiple solution branches have been identified in the symmetric case, they can be traced continuously as the wind stress geometry or basin shapes are modified in a continuous way.

The multiple dynamical regimes identified in the studies of McCalpin and Haidgovel (1996) and Spall (1996b) were obtained for basin sizes with larger zonal than meridional extent, while our calculations used a basin with a north–south extent twice as large as its east–west extent. We are currently exploring the effect of different basin sizes as well as nonsymmetric wind stress curl profiles on the bifurcation structure of the model. Work on the link between multiple equilibria of a model with the same configuration as that used by McCalpin and Haidgovel (1996) and the preferred dynamical regimes they found is in progress.

APPENDIX A

Method of Solution

The governing equation is discretized using finite differences on a nonuniform rectangular grid with N_x grid points in the x direction and N_y grid points in the y direction. The scheme is made to be second-order accurate on the nonuniform grid by using a method outlined in Marti et al. (1992). The physical coordinates (x, y) are given terms of the computational coordinates $\{(i, j) \mid i = 1, 2, \cdots, N_y \text{ and } j = 1, 2, \cdots, N_x\}$ by the following formulas:

$$x = \frac{X(j)^3 - m_x X(j)}{1 + m_x}, \quad \text{and} \quad y = \frac{Y(i)^3 + m_y Y(i)}{1 + m_y}, \tag{A1}$$

where

$$X(j) = \frac{j - 1}{N_x - 1},$$

and

$$Y(i) = \frac{i - (N_y - 1)/2 + 1}{N_y - 1}. \tag{A2}$$

The quantities m_x and m_y are adjustable parameters that control the degree to which grid lines are concentrated near the western boundary and near the line of zero wind stress curl. The Jacobian is discretized using Arakawa's (1966) formulation with the appropriate modification for the nonuniform grid spacing (Salmon and Talley 1988). The potential vorticity on the boundary is treated as an unknown that must be solved as part of the solution. The no-flux boundary conditions are treated using second-order accurate centered differences. After discretization, the PDE is expressed as a coupled system of nonlinear ordinary differential equations for the time-dependent case and a coupled system of nonlinear algebraic equations for the steady case. There is one unknown for each grid point that can be organized into a state vector, **u**. Elements of **u** corresponding to grid points in the interior of the domain are the values of ψ evaluated at the interior grid points and those elements of **u** corresponding to grid points on the boundary of the domain are the values of ζ evaluated at the boundary grid points. The discretized equation for the steady state can be written as follows:

$$\mathbf{F}(\mathbf{u}; \delta_I, \delta_S, \delta_H) = 0. \tag{A3}$$

The steady-state solutions are found using an arclength predictor–corrector continuation algorithm. An Euler predictor step is used as an initial estimate of the solution, followed by an iterative Newton corrector. The solution branches are parameterized using pseudoarclength continuation (Seydel 1994), which allows the solution branches to be traced past singular

points. Bifurcation points leading to multiple equilibria can be detected by monitoring the sign of the determinant of the Jacobian matrix of partial derivatives of the discretized system of equations. Hopf bifurcation points are detected by a linear stability analysis. This is accomplished by looking for eigenmodes of the form

$$\psi'(x, y, t) = e^{\sigma t}\phi(x, y). \tag{A4}$$

Substitution of the modal form into the linearized problem yields the equation

$$\sigma\nabla^2\phi + J(\psi_s, \delta_I^2\nabla^2\phi) + J(\phi, \delta_I^2\zeta_s + y)$$
$$= -\delta_S\nabla^2\phi - \delta_H^5\nabla^4(\nabla^2\phi), \tag{A5}$$

where ψ_s is the steady-state equilibria. Unstable eigenmodes have eigenvalues with positive real part, and stable eigenmodes have eigenvalues with negative real part. A Hopf bifurcation occurs when a pair of complex conjugate eigenvalues crosses the imaginary axis and all other eigenvalues are stable (i.e., to the left of the imaginary axis). The discretized linear stability equation can be rewritten in matrix form as a generalized eigenvalue problem:

$$\mathbf{F_u v} = \sigma\mathbf{L v}. \tag{A6}$$

Here $\mathbf{F_u}$ is the Jacobian matrix of partial derivatives and $\mathbf{L}$ is a discretized version of the Laplacian operator. The discretized eigenmode is given by $\mathbf{v}$, and its eigenvalue is given by σ. The goal is to find the eigenvalue with the largest real part, so that one can detect if a Hopf bifurcation as occurred as one of the equation's parameters is varied. A method introduced by Neubert (1993) is used to efficiently solve the above problem. The method consists of a predictor–corrector strategy to follow the curve of the dominant eigenvalue μ as a function of one of the parameters. A subsequent computation is used to detect the possibility of the occurrence of an exchange of roles whereby an eigenvalue not being followed becomes dominant with respect to the real part.

APPENDIX B

Convergence and Grid Resolution

In this section, the issue of convergence of the steady-state solutions as the grid resolution is increased is discussed. Some of the computations were repeated using a uniform grid with half and twice as many grid points in both the x and y direction. The three grids had (33×17), (65×33), and (129×65) grid points in the x and y directions. In all the computations δ_S and δ_H are fixed at 0.01 and 0.04, respectively.

The bifurcation structure is not changed qualitatively in going from a 33×17 gridpoint model to a $129 \times$ 65 gridpoint model. The coarse resolution model with only 33×17 grid points is sufficient to capture the

TABLE B1. Comparison of the location of the bifurcation points for $\delta_S = 0.01$ and $\delta_H = 0.04$, computed on three grids with uniform grid point spacing and with 33×17, 65×33, and 129×65 grid points in the y and x directions. Column 3 gives $O(h^2)$ estimate for the location of the bifurcation points. Column 4 gives the relative difference of the location of the bifurcation points calculated on the different grids.

Bifurcation point	Resolution	δ_I	
		$O(h^2)$	Relative difference
PF N1	33×17	0.0362	
			2%
	65×33	0.0334	
			0.5%
	129×65	0.0340	
PF N2	33×17	0.0743	
			0.2%
	65×33	0.0737	
			0.1%
	129×65	0.0734	
Hopf 1	33×17	0.0762	
			0.6%
	65×33	0.0743	
			0.1%
	129×65	0.0740	
Hopf 2	33×17	0.1720	
			3%
	65×33	0.1522	
			1%
	129×65	0.1514	
PF N3	33×17	0.1416	
			8%
	65×33	0.0991	
			<0.1%
	129×65	0.0990	
PF N3	33×17	0.1577	
			7%
	65×33	0.1145	
			0.1%
	129×65	0.1140	

existence of all the bifurcations of the antisymmetric branch found using the higher-resolution model with 129×65 grid points. Table B1 shows that the discretized model appears to be converging quantitatively as the grid spacing is reduced.

REFERENCES

Arakawa, A., 1966: Computational design for long-term numerical integration of the equations of fluid motion: Two-dimensional incompressible flow. Part I. *J. Comput. Phys.,* **1,** 119–143.

Berloff, P., and S. P. Meacham, 1997: The dynamics of an equivalent-barotropic model of the wind-driven circulation. *J. Mar. Res.,* **55** (3), 407–451.

Brown, O. B., and R. H. Evans, 1987: Satellite infrared remote sensing. *Study of Physical Processes on the U.S. Mid-Atlantic Slope and Rise,* Casagrande, Ed., Science Applications International, IV-67–IV-97.

Cessi, P., and G. R. Ierley, 1995: Symmetry-breaking multiple equi-

libria in quasigeostrophic, wind-driven flows. *J. Phys. Oceanogr.,* **25,** 1196–1205.

Harrison, D. E., and W. R. Holland, 1981: Regional eddy vorticity transport and the equilibrium vorticity budgets of a numerical model ocean circulation. *J. Phys. Oceanogr.,* **11,** 190–208.

Ierley, G. R., and V. Sheremet, 1995: Multiple solutions and advection-dominated flows in the wind-driven circulation. Part I: Slip. *J. Mar. Res.,* **53** (5), 703–737.

Jiang, S., F. Jin, and M. Ghil, 1995: Multiple equilibria, periodic, and aperiodic solutions in a wind-driven, double-gyre, shallow-water model. *J. Phys. Oceanogr.,* **25,** 764–786.

Legras, B., and M. Ghil, 1985: Persistent anomalies, blocking and variations in atmospheric predictability. *J. Atmos. Sci.,* **42,** 433–471.

Marshall, J. C., 1984: Eddy–mean-flow interaction in a barotropic ocean model. *Quart. J. Meteor. Soc.,* **110** (465), 573–590.

Marti, O., G. Madsec, and P. Delecluse, 1992: Comment on ''Net diffusivity in ocean general circulation models with nonuniform grids'' by F. L. Yin and I. Y. Fung. *J. Geophys. Res.,* **97,** 12 763–12 766.

McCalpin, J. D., and D. B. Haidgovel, 1996: Phenomenology of the low-frequency variability in a reduced gravity, quasigeostrophic double-gyre model. *J. Phys. Oceanogr.,* **26,** 739–752.

Meacham, S. P., and P. S. Berloff, 1997: Barotropic, wind-driven circulation in a small basin. *J. Mar. Res.,* **55** (3), 523–563.

Neubert, R., 1993: Predictor–corrector techniques for detecting Hopf bifurcation points. *Int. J. Bifurcation and Chaos,* **3** (5), 1311–1318.

Olson, D. B., G. Podestá, R. H. Evans, and O. Brown, 1988: Temporal variations in the separation of Brazil and Malvinas currents. *Deep-Sea Res.,* **35,** 1971–1990.

Pedlosky, J., 1996: *Ocean Circulation Theory.* Springer-Verlag, 453 pp.

Salmon, R., and L. D. Talley, 1988: Generalizations of Arakawa's Jacobian. *J. Comput. Phys.,* **83,** 247–259.

Seydel, R., 1994: *Practical Bifurcation and Stability Analysis: From Equilibrium to Chaos.* Vol. 5. *Interdisciplinary Applied Mathematics,* Springer-Verlag, 407 pp.

Spall, M. A., 1996a: Dynamics of the Gulf Stream/deep western boundary current crossover. Part I: Entrainment and recirculation. *J. Phys. Oceanogr.,* **26,** 2152–2168.

——, 1996b: Dynamics of the Gulf Stream/deep western boundary current crossover. Part II: Low-frequency internal oscillations. *J. Phys. Oceanogr.,* **26,** 2169–2182.

Speich, S., H. Dijkstra, and M. Ghil, 1995: Successive bifurcations in a shallow-water model applied to the wind-driven ocean circulation. *Nonlinear Processes Geophys.,* **2,** 241–268.

Taft, B. A., 1972: Characteristics of the flow of the Kuroshio south of Japan. *Kuroshio, Physical Aspects of the Japan Current*, H. Stommel and K. Yoshida, Eds., University of Washington Press, 165–214.

Veronis, G., 1966: Wind-driven circulation—Part 2. Numerical solutions of the non-linear problem. *Deep-Sea Res.,* **13** (2), 31–55.